

# Strain-Engineered Metal-Free h-B<sub>2</sub>O Monolayer as a Mechanocatalyst for Photocatalysis and Improved Hydrogen Evolution Reaction

Xiaofeng Zhao, Xiaoyong Yang,\* Deobrat Singh, Pritam Kumar Panda, Wei Luo, Yuxiang Li, and Rajeev Ahuja\*



Cite This: *J. Phys. Chem. C* 2020, 124, 7884–7892



Read Online

ACCESS |



Metrics & More

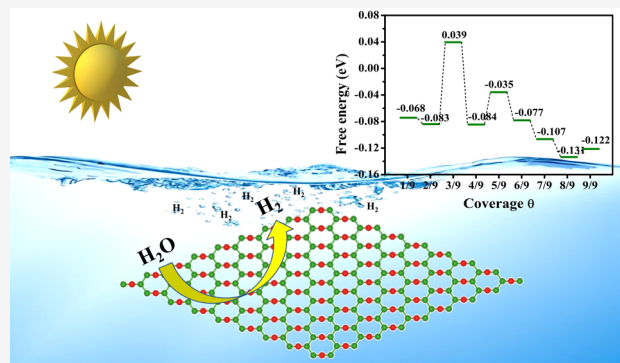


Article Recommendations



Supporting Information

**ABSTRACT:** Developing stable metal-free materials with a highly efficient hydrogen evolution reaction (HER) has received intense research interest due to its renewable and environmentally friendly properties. In this work, we systematically investigated the HER catalytic activity of a new h-B<sub>2</sub>O monolayer based on first-principles calculations. The results show the B site in the h-B<sub>2</sub>O structure is energetically favorable for hydrogen with the calculated Gibbs free energy ( $\Delta G_{H^*}$ ) of  $-0.07$  eV, which is comparable to that of the Pt catalyst ( $\Delta G_{H^*} = -0.09$  eV). Moreover, the catalytic activity of the h-B<sub>2</sub>O monolayer is quite robust with increasing hydrogen coverages (from 1/9 to 9/9). Interestingly, the HER activity of the h-B<sub>2</sub>O monolayer is sensitive to the strains-driven. For example, applied tensile strains (0–2%) could weaken the bonding between hydrogen and the substrate, resulting in  $\Delta G_{H^*}$  even close to 0 eV. However, the opposite trend is found for applied compressive strain. After analyzing the density of states (DOS), we found the h-B<sub>2</sub>O monolayer with absorbed hydrogen retains the metallic property, still exhibiting excellent electrical conductivity. These results reveal that the metal-free h-B<sub>2</sub>O monolayer is a promising candidate for HER applications.



## 1. INTRODUCTION

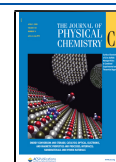
Renewable energy especially for green hydrogen energy, including H<sub>2</sub> and hydrogen-containing compounds, is the main candidate alternative to fossil fuels due to air pollution by carbon/nitrogen dioxide emissions. Thus, the sustainable and efficient hydrogen energy exhibits the potential applications in energy storage, energy production, energy conversion, electricity, and heating or cooling effect in building, which is imperative for the current circular economy and ecological environment. Among series of process production, water splitting to generate H<sub>2</sub> is gaining credibility, in which there are two important reactions: (1) hydrogen evolution reaction (HER) at the anode and (2) oxygen evolution reaction (OER) at cathode.<sup>1–4</sup> So far, Pt-based alloys or compositions have shown extraordinary catalytic performance for driving the HER to H<sub>2</sub> generation due to the lower migration potential of the electron–hole pair on the reaction surface.<sup>5,6</sup> However, the scarcity and nonrenewable property of Pt material with its high cost limit its large-scale application in the industry. Up to now, hydrogen energy accounts for less than 5% of annual energy consumption, inciting the scientists to further study and design more effective catalysts to promote the application of this renewable energy.

Successful delamination of graphene brings the application potential of low-dimension materials as photocatalysts, electrodes, sensors, and photodetectors due to their unique physical and chemical properties compared with those of conventional bulk materials, such as high specific surface activity, novel electronic, adjustable band gap, strong charge transfer, etc.<sup>7–19</sup> Until now, series of two-dimensional (2D) materials have been successfully synthesized including graphene oxides,<sup>13,20,21</sup> g-C<sub>3</sub>N<sub>4</sub>,<sup>22–26</sup> borophene,<sup>7,27</sup> traditional metal dichalcogenides (TMDs),<sup>28,29</sup> and MXenes,<sup>28–30</sup> among which metal-free-based materials appear as interesting options because of their renewable and environmentally friendly properties. In regard to 2D carbonaceous materials, doping engineering is the dominant approach to improve the catalytic activity, such as Au doping graphene,<sup>20</sup> Cu/Co/Fe doping g-C<sub>3</sub>N<sub>4</sub>,<sup>31,31</sup> Ag<sub>2</sub>CrO<sub>4</sub>/g-C<sub>3</sub>N<sub>4</sub>/graphene.<sup>32</sup> For the neighboring element

Received: January 30, 2020

Revised: March 14, 2020

Published: March 16, 2020



to carbon according to the periodic table of elements, boron monolayer or borophene has attracted abundant attention due to its metallic feature with a strong complementary electronic structure similar to that of graphene.<sup>33</sup> As demonstrated by several reports, borophene monolayer is competitive with Pt as a catalyst in photocatalysis water splitting.<sup>7,34</sup> However, the stable borophene nanosheets should be grown on Ag surface (111) under vacuum condition, since it is easily oxidized if exposed to air, subsequently changing its initial structure and decreasing the catalytic activity.<sup>35</sup> To explore the possible applications of boron-based 2D materials, B<sub>3</sub>S nanosheets with a four-layer structure are synthesized by the method of Wu et al.,<sup>36</sup> where the S atoms are located at the top and the bottom layers and the middle two layers are occupied by B atoms. This stable B<sub>3</sub>S nanosheet shows a promising performance for photocatalysis with desirable values ( $\Delta G_{H^*}$ ) of 0.30 eV with hydrogen coverage  $\theta$  as 1/8, revealing the intrinsically high catalytic activity. Besides, several previous works reported the oxidation processes of borophene materials, which were controlled by the ratio of oxygen incorporated into the initial borophene structure.<sup>35,37–41</sup> A series of borophene oxide compounds, such as B<sub>4</sub>O, B<sub>5</sub>O, B<sub>6</sub>O, B<sub>7</sub>O, and B<sub>8</sub>O structures, were successfully proposed, in which it is found that the structures of B<sub>5</sub>O, B<sub>7</sub>O, and B<sub>8</sub>O with metallic quality present a strong conductivity anisotropy and the structure of B<sub>6</sub>O exhibits a Dirac loop near the Fermi level.<sup>37</sup> Very recently, a novel h-B<sub>2</sub>O monolayer was proposed based on the honeycomb borophene that was synthesized on the Al(111) substrate.<sup>27,42</sup> Under the prediction by first-principles calculations, the h-B<sub>2</sub>O monolayer is mechanically stable with anisotropy property and also exhibits as a Dirac material, unveiling that the oxidation process is a valid method to stabilize the boron monolayer. Naturally, someone may wonder how does oxidation stabilization engineering affects the catalytic activity of the borophene monolayer?

Motivated by the above question, the purpose of this work is to investigate whether the borophene oxide (h-B<sub>2</sub>O) can act as a potential photocatalyst for HER. After comprehensive calculations, we find that the h-B<sub>2</sub>O monolayer shows metallic property with or without a hydrogen adatom. The B sites are confirmed as the highly active sites for HER, and defect engineering could reduce the pristine catalytic efficiency. Importantly, the Gibbs free energy ( $\Delta G_{H^*}$ ) of −0.07 eV is obtained through density functional theory (DFT) calculations, which is comparable to that of the Pt catalyst. We further explore the influence of hydrogen concentration and strains on HER activity. Applying tensile strains (1–1.5%) at hydrogen coverages of 1/9 drive  $\Delta G_{H^*}$  even close to 0 eV, indicating that the h-B<sub>2</sub>O monolayer is a promising material for photocatalysis.

## 2. COMPUTATIONAL METHOD

Our calculations were performed using density functional theory (DFT) as implemented in Vienna ab initio program package (VASP) code.<sup>43,44</sup> We used the frozen-core projector augmented wave (PAW) method<sup>45</sup> to deal with nuclei and core electrons, where B is 2s<sup>2</sup>2p<sup>1</sup>, O is 2s<sup>2</sup>2p<sup>4</sup>, and H is 1s<sup>1</sup>. The generalized gradient approximation based on the Perdew–Burke–Ernzerhof (PBE)<sup>46</sup> functional was used to describe exchange–correlation interactions.<sup>47</sup> Besides, the van der Waals interaction (vdW) was considered in all calculation processes with the zero-damped DFT + D<sub>3</sub> proposed by Grimme.<sup>48</sup> A 20 Å vacuum space in the z-direction is inserted

to prevent the interaction between repeated slabs. Plane waves with a 540 eV cutoff energy is applied to explain the electron wave functions. For the convergence tolerance in structural relaxation, 0.001 eV/Å and 10<sup>−5</sup> eV are set for the residual forces and energy on per atom, respectively. The Brillouin zone is sampled by 11 × 11 × 1 for the unit cell and 3 × 3 × 1 for 3 × 3 × 1 supercell for the total energy calculations. We set 0.01 eV for the smearing values based on the Gaussian smearing to describe the electronic occupancy. To correctly describe the band structures, the Heyd–Scuseria–Ernzerhof (HSE06) method<sup>49</sup> was performed in Band and DOS calculations. Moreover, the charge distribution and transfer based on the Bader charge approach were applied to understand the interaction of hydrogen and the h-B<sub>2</sub>O monolayer. The stability was investigated using the NVT ensemble at *T* = 300 K via the Nosé–Hoover method.<sup>50</sup> Additionally, for comparison with empirical vibrational energy, the average kinetic energy was calculated via the following eq 1<sup>51</sup>

$$E = \frac{3}{2} N k_B T \quad (1)$$

where *N* is the atom number in the system, *k<sub>B</sub>* is the Boltzmann constant, and *T* is the absolute temperature defined by the current calculation.

For the h-B<sub>2</sub>O monolayer with adatom hydrogen, the binding energy ( $\Delta E_{H^*}$ ) is given according to the following equation<sup>5</sup>

$$\Delta E_{H^*} = \frac{1}{n} (E_{BO+H^*} - E_{BO} - \frac{n}{2} E_{H_2}) \quad (2)$$

where *n* denotes the number of hydrogen atoms on the h-B<sub>2</sub>O monolayer. *E<sub>BO+H\*</sub>* and *E<sub>BO</sub>* are the energy with and without hydrogen atoms, respectively. The asterisk (\*) is the active site (the most stable adsorption position) on the h-B<sub>2</sub>O monolayer. Subsequently, the Gibbs free energy can be calculated by eq 3<sup>5</sup>

$$\Delta G_{H^*} = \Delta E_{H^*} + \Delta E_{ZPT} - T \Delta S_{H^*} \quad (3)$$

where  $\Delta E_{ZPT}$  and  $\Delta S_{H^*}$  are the differences of the zero-point energy and the entropy between adsorption hydrogen and gas phase (adsorption H<sub>2</sub>), respectively. Generally,  $\Delta E_{ZPT}$  and  $\Delta S_{H^*}$  have small values. Specifically,  $\Delta E_{ZPT}$  is defined as<sup>52</sup>

$$\Delta E_{ZPT} = E_{ZPT}^{nH} - E_{ZPT}^{(n-1)H} - \frac{1}{2} E_{ZPT}^{H_2} \quad (4)$$

where  $E_{ZPT}^{nH}$  is the zero-point energy of *n* hydrogen atoms on the h-B<sub>2</sub>O monolayer and the  $E_{ZPT}^{H_2}$  is the zero-point energy of H<sub>2</sub> molecule in the gas phase.  $\Delta S_{H^*}$  is defined as<sup>3</sup>  $T \Delta S_{H^*} = TS_{H^*} - 1/2 TS_0$ , where *TS<sub>H\*</sub>* is the vibrational entropy of the hydrogen adatom on the h-B<sub>2</sub>O monolayer, which has been confirmed to be 0.026 eV at 300 K.<sup>53</sup> The *S<sub>0</sub>* presents the vibrational entropy of the H<sub>2</sub> molecule, and the value of *TS<sub>0</sub>* is given as 0.41 eV.<sup>5</sup> Thus, the value of  $\Delta E_{ZPT} - T \Delta S_{H^*}$  is 0.248 eV for hydrogen adsorption on the h-B<sub>2</sub>O monolayer. The criterion of an ideal HER activity is  $\Delta G_{H^*}$  approximately equal to 0 eV. The positive value denotes relatively slow kinetics in the process of hydrogen adsorption, while the negative value presents relatively slow kinetics in the process of H<sub>2</sub> release.<sup>52,54</sup>

The exchange current was analyzed based on Nørskov's assumption.<sup>5</sup> For  $\Delta G_{H^*} < 0$ , the expression of exchange current at pH = 0 is expressed as

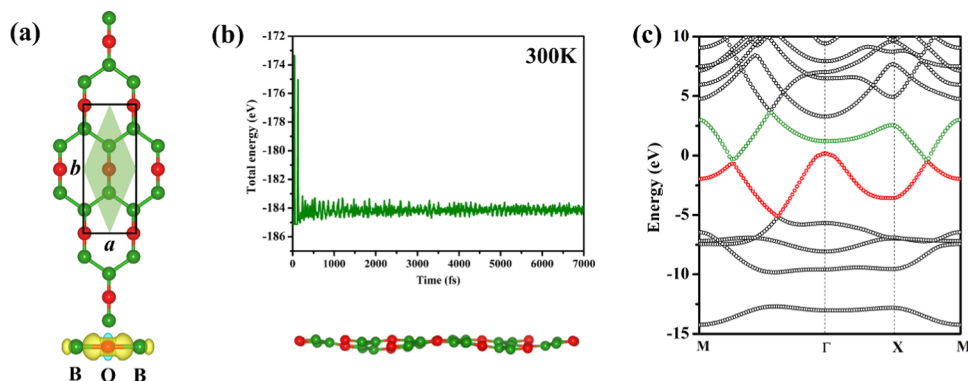


**Figure 1.** (a) Top view showing the h-B<sub>2</sub>O monolayer structure, where the green shadowed area and the orthogon stand for the primitive cell and conventional cell, respectively. The side view showing the differential charge density of the primitive cell. (b) Total energy fluctuation of the h-B<sub>2</sub>O monolayer at 300 K in ab initial dynamics simulation (AIMD) simulation. The bottom view showing the h-B<sub>2</sub>O configuration after 7 ps. (c) Calculated band structure of the h-B<sub>2</sub>O monolayer based on HSE06 methods.

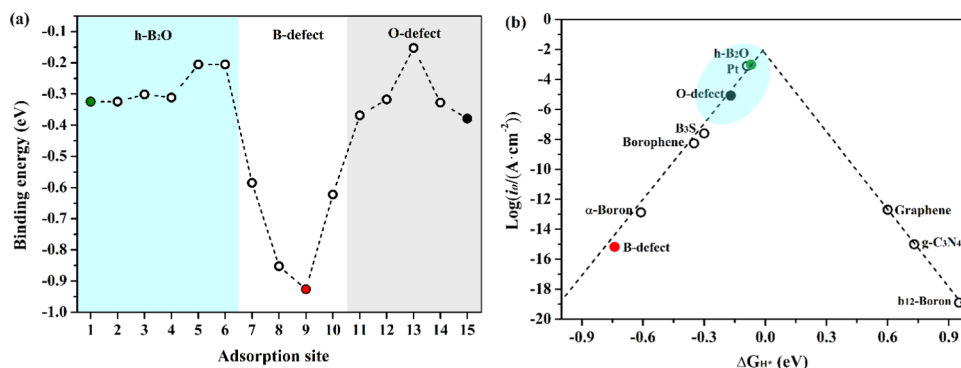


**Figure 2.** (a) Binding energy of the hydrogen adsorbed on the possible sites for the pristine h-B<sub>2</sub>O monolayer and B/O defective models, respectively. (b) HER volcano curve including the h-B<sub>2</sub>O monolayer and B/O defective models corresponding to the colored dots in (a). Besides, the results of other boron materials,<sup>36,58,59</sup> g-C<sub>3</sub>N<sub>4</sub>,<sup>60,61</sup> graphene,<sup>61</sup> and Pt catalysts<sup>5</sup> are presented for comparison.

$$i_o = -ek_o \frac{1}{1 + \exp\left(-\frac{\Delta G_{H^*}}{k_B T}\right)} \quad (5)$$

For  $\Delta G_{H^*} > 0$ , the exchange current was calculated by

$$i_o = -ek_o \frac{1}{1 + \exp\left(\frac{\Delta G_{H^*}}{k_B T}\right)} \quad (6)$$

where  $k_o$  is the rate constant and  $k_B$  is the Boltzmann constant.

Moreover, the effect of B/O defects on the catalyst efficiency was also discussed in eqs 2–7. The formation energy of the B/O vacancy defects is defined as

$$\Delta E_f = -(E_{BO} - E_{Vi} - u_i) \quad (7)$$

where  $E_{BO}$  is the total energy of pristine B<sub>2</sub>O.  $E_{Vi}$  shows the energy of the B<sub>2</sub>O monolayer with a B/O vacancy defect.  $u_i$  is the corresponding chemical potentials of B and O elements in tetragonal boron (P4<sub>2</sub>/nm) and O<sub>2</sub> gas, respectively. After calculation, the formation energies of the B/O vacancy defect are 1.3 and 5.8 eV, respectively.

### 3. RESULTS AND DISCUSSION

**3.1. Structural Property and Stability.** The primitive cell of h-B<sub>2</sub>O comprises one O atom and two B atoms with the Cmmm (No. 65) space group,<sup>42</sup> as shown in Figure 1a. The calculated lattice parameters are 2.806 Å for *a* and 7.127 Å for *b*, respectively. The B–O bond length is obtained as 1.339 Å.

Three different angles are found in one honeycomb: approximately 180° for ∠B–O–B, 110° for ∠B–B–B, and 125° for ∠B–B–O. Previous studies demonstrated that the extraordinary physical and chemical properties of borophene are derived from the highly anisotropic structure by triple bonded B atoms.<sup>35,38</sup> In the h-B<sub>2</sub>O monolayer, the buckled structure is still exhibited. As presented in Figure 1a, the buckled structure inherits from the parental borophene (h-B) with a lower symmetry due to oxygen doping, which extends the mechanical anisotropy of the (h-B) monolayer as reported by a previous study.<sup>42</sup>

The dynamical stability of the h-B<sub>2</sub>O monolayer was investigated by ab initial dynamics simulation (AIMD) based on the Nosé thermostat algorithm with the 300 K isothermal field. The calculated results are displayed in Figure 1b. One can see the total energy tends to smoothen the fluctuation in the energy region from −184.5 to −183.4 eV after 300 fs relaxation. The average energy of per atom is approximate 0.03 eV in the h-B<sub>2</sub>O system, which agrees with the average translational energy of per atom for bulk material deduced by  $3kT/2$ . Responding to temperature effect, the h-B<sub>2</sub>O monolayer distorted slightly with a maximum height difference of 0.803 Å, implying it is dynamical stable with high toughness. Notably, the thermal stability of the h-B<sub>2</sub>O monolayer has been demonstrated based on the phonon spectrum, in which no negative mode was observed for the whole Brillouin zone.<sup>42</sup>

The calculated sophisticated hybrid function (HSE) band in Figure 1c shows that the h-B<sub>2</sub>O monolayer is a Dirac material



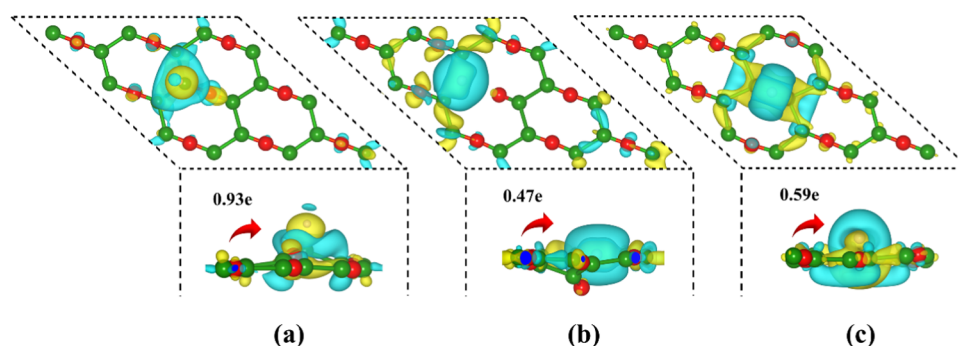


**Figure 3.** Charge density difference for the advantageous location of the hydrogen atom in (a) pristine h-B<sub>2</sub>O monolayer, (b) B-defect monolayer, and (c) O-defect monolayer. The yellow (cyan) area presents charge accumulation (depletion). The red arrows show the orientation and the value of charge transfer of hydrogen.

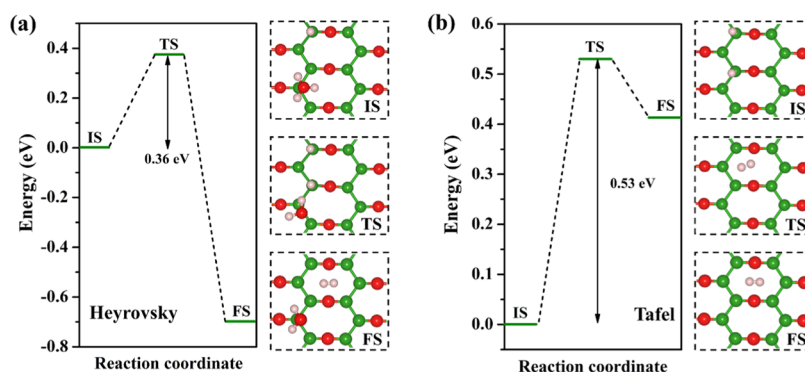


**Figure 4.** Energy landscape of the Heyrovsky (a) and the Tafel (b) reactions on the h-B<sub>2</sub>O monolayer including the reaction coordinate structure of the initial state (IS), transition state (TS), and final state (FS).

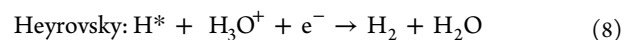
with a Dirac cone located in the  $X \rightarrow M$  path. The corresponding band structure using the PBE method is shown in Figure S1, which shows a similar track compared with the HSE band. These results reveal the strong metallicity of the h-B<sub>2</sub>O monolayer. The existential Dirac cone provides a unique transporting path for the conduction band minimum (CBM) to capture the excited electrons from valence band maximum (VBM), which will reduce the combination rates of holes and excited electrons on the VBM and further enhance the catalytic performance for HER. More importantly, the projected band of the h-B<sub>2</sub>O monolayer in Figure S2 reveals that the Dirac cone is mainly contributed by  $s$  and  $p_z$  orbitals of the B atom and  $p_y + p_z$  orbitals of the O atom. These orbitals are saturated, leading to a relatively weak binding energy between the h-B<sub>2</sub>O monolayer and adatoms. From the projected density of states (PDOS) in Figure S3, one can see that the stable  $p_x$  orbitals of the B and O atoms are mainly located in the low-energy region ( $-10$  to  $-5$  eV) with a strong hybridization with  $p_y$  and  $p_z$  orbitals. By Bader analysis, it is found O atom gains 2.04 e from the adjacent B atom. It clearly elucidates that the compensated electrons in the low-energy orbital of the O atom could stabilize the electronic structure of the h-B<sub>2</sub>O monolayer.

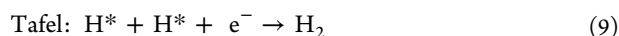
**3.2. HER Activity.** To reveal the catalytic performance of the h-B<sub>2</sub>O monolayer, we investigate the active site on the  $3 \times 3 \times 1$  supercell with and without defect. Fourteen possible adsorption sites for hydrogen are considered, as shown in Figure S4, including the top sites of the B/O atom, top sites of the B/O vacancy, and hexagonal center and bridge site between B and B/O atoms (B–B, B–O). For the pristine h-B<sub>2</sub>O monolayer, the calculated binding energy in Figure 2a

shows that the most advantageous site for HER is the top of the B atom with the Gibbs free energy ( $\Delta G_{H^*}$ ) of  $-0.07$  eV. Besides, the B defect engineering shows a strong interaction with the adsorbed hydrogen ( $\Delta G_{H^*} = -0.74$  eV), hindering the release of H<sub>2</sub>. While the O defect structure is less favorable to adsorb hydrogen with  $\Delta G_{H^*}$  of  $-0.17$  eV.

The Bader analysis in Figure 3 shows that the adsorbed hydrogen atom gains 0.96, 0.47, and 0.59 e from the defect-free, B, and O vacant h-B<sub>2</sub>O monolayer, respectively, which suggests that charge transfer occurs in the adsorption process. For the pristine monolayer, a larger number of electrons are transferred from the h-B<sub>2</sub>O monolayer to H<sup>\*</sup>, even close to the chemical saturation charge of hydrogen (H<sup>+</sup>). Interestingly, the obtained Gibbs free energy decreases with the increasing charge transfer to H<sup>\*</sup>, suggesting the intensity of charge transfer is responsible for the catalytic activity in HER. Importantly, it is worth mention that oxidation engineering not only could improve the mechanical stability of boron monolayer but also is an effective method to enhance the catalytic activity of HER, as compared with the borophene ( $\Delta G_{H^*} = -0.35$  eV)<sup>49</sup> and B<sub>3</sub>S nanosheets ( $\Delta G_{H^*} = -0.30$  eV).<sup>30</sup>

The Heyrovsky and Tafel reactions for the HER process under pH 0 environment were further investigated to understand the reaction mechanism of producing H<sub>2</sub> on the h-B<sub>2</sub>O monolayer. Three states were considered in both reactions, including the initial state (IS), transition state (TS), and final state (FS). Specifically, the Heyrovsky and Tafel reactions are presented by<sup>21</sup>





For the Heyrovsky reaction,  $\text{H}_2$  is produced when adsorbed hydrogen ( $\text{H}^*$ ) interacts with  $\text{H}_3\text{O}^+$  clusters. The reaction barrier is determined by the breaking away of a proton from the  $\text{H}_3\text{O}^+$  cluster. As shown in Figure 4a, the calculated energy barrier for the Heyrovsky pathway is 0.36 eV. Subsequently, the generated  $\text{H}_2$  molecules move to the cavity center of the h- $\text{B}_2\text{O}$  monolayer, which could accelerate the release rate. For the Tafel reaction, the activation energy barrier is 0.53 eV. Meanwhile, the ground state energy of FS is higher than that of IS, which would decrease the  $\text{H}_2$  release rate. Thus, the HER mechanism of the h- $\text{B}_2\text{O}$  monolayer may follow the Heyrovsky-dominated Volmer–Heyrovsky reaction.

**3.3. Effects of Hydrogen Coverage.** Generally, the HER activity characterized by Gibbs free energy ( $\Delta G_{\text{H}^*}$ ) is sensitive to hydrogen coverage.<sup>34,55</sup> Coverage control avails release the hydrogen molecules from the surface of materials by turning binding energy and then improve the catalytic efficiency. Thus, a series of adsorption models with different hydrogen coverages from 1/9 to 9/9 were investigated in this work. The most stable adsorption sites are shown in Figure S6. The calculated coverage-dependent  $\Delta G_{\text{H}^*}$  is presented in Figure 5.

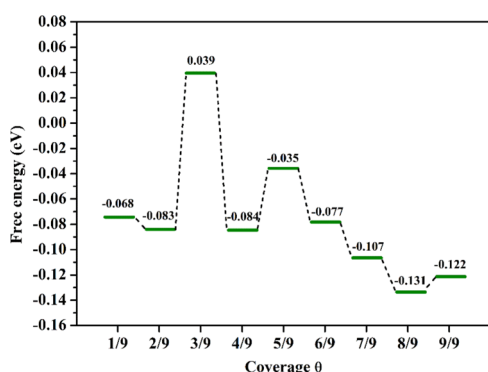


**Figure 5.** Calculated Gibbs free energy along the hydrogen coverage by PBE methods. Hydrogen atoms adsorbed on an advantageous location in the h- $\text{B}_2\text{O}$  monolayer.

For h- $\text{B}_2\text{O}$  with 1/9 coverage,  $\Delta G_{\text{H}^*}$  is  $-0.068$  eV, revealing a perfect HER catalytic. When the hydrogen coverage further reaches 3/9, the HER activity is clearly enhanced with  $\Delta G_{\text{H}^*}$  of 0.039 eV. The hydrogen coverage of 5/9 gives rise to the highest HER catalytic performance with  $\Delta G_{\text{H}^*}$  of  $-0.035$  eV. However, the  $\Delta G_{\text{H}^*}$  is significantly decreased as hydrogen coverage increases beyond 7/9 due to the strong binding with substrate h- $\text{B}_2\text{O}$ . Notably,  $\Delta G_{\text{H}^*}$  with hydrogen coverage of 2/9, 4/9, and 6/9 ranges from  $-0.084$  to  $-0.077$  eV, which is slightly lower than that of 1/9. We can conclude that the h- $\text{B}_2\text{O}$  monolayer under 6/9 hydrogen coverage shows good HER performance. The charge transfer based on the Bader charge analysis can well explain the HER activity affected by hydrogen coverage. As shown in Table S1, fewer electrons are transferred to  $\text{H}^*$  under 6/9 coverage, while more electrons are transferred to  $\text{H}^*$  under 7/9–9/9 coverage. It indicates that a lower coverage gives rise to a relatively weaker B–H binding energy, which could accelerate the  $\text{H}_2$  release from the h- $\text{B}_2\text{O}$  monolayer. The overall  $\Delta G_{\text{H}^*}$  ranging from  $-1.131$  to 0.039 eV reveals that the h- $\text{B}_2\text{O}$  monolayer possesses a superexcellent HER activity over a wide range of H coverage.

To understand the variation of binding energy affected by hydrogen coverage, we investigated the total density of states (TDOS) and projected density of states (PDOS) for the h- $\text{B}_2\text{O}$  monolayer with adsorbed hydrogen atoms, along with the corresponding work functions. As depicted in Figure 6, the

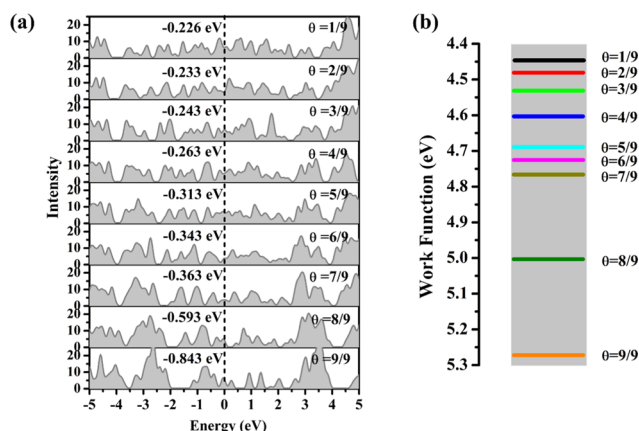


**Figure 6.** Density of states (a) and work functions (b) for the h- $\text{B}_2\text{O}$  monolayer with adsorbed hydrogens. The black dashed line denotes the Fermi level position.

TDOS peaks for all considered hydrogen coverage systems distinctly cross the Fermi level with relatively strong intensity, mainly benefitting from B atoms (as shown in Figure S7), which thus should be rich in active sites for catalysis. Moreover, we notice that the Fermi level moves toward the lower energy in the range of  $-0.203$  to  $-0.843$  eV with increasing hydrogen coverage, which agrees well with the  $\text{B}_3\text{S}$  monolayer affected by hydrogen coverage.<sup>36</sup> As evidenced by PDOS in Figure S7, the activity of H 1s mainly locates from  $-4$  to  $-1$  eV with increasing hydrogen coverage. Specifically, more electrons from the B atom move to these energy levels to hybridize with hydrogen atoms with an increase in hydrogen coverage. This trend strongly reveals the interaction between hydrogen and the h- $\text{B}_2\text{O}$  monolayer. Interestingly, enhanced interaction would result in the slow release of electrons from the h- $\text{B}_2\text{O}$  monolayer surface, in accordance with the above results in Figure 6b. Moreover, the work function of the h- $\text{B}_2\text{O}$  monolayer slightly increases, ranging from 4.45 to 4.73 eV, when the hydrogen coverage is less than 7/9.

**3.4. Tuning HER Activity by Strain-Driven.** Another method to shift the redox band level with optimization of the HER activity is to apply an external strain.<sup>56,57</sup> Therefore, we investigated the strain effects from  $-2$  to 2% on the HER activity of the h- $\text{B}_2\text{O}$  monolayer. The strain is defined as  $\delta = (\lambda_1 - \lambda)/\lambda$ , where  $\lambda_1$  and  $\lambda$  are the lattice parameters of the supercell with and without deformation, respectively. Hence,  $-2$  to 0% presents the compressive strain and 0 to 2% signifies the tensile strain. The light blue background in Figure 7 presents the HER activity of Pt ( $-0.09$  eV). Clearly, it is observed that increasing the tensile strain results in a more positive  $\Delta G_{\text{H}^*}$  for the coverage ranging from 1/9 to 6/9, but it decreases  $\Delta G_{\text{H}^*}$  for the hydrogen coverage ranging from 7/9 to 9/9, as shown in Figure 7a. Interestingly,  $\Delta G_{\text{H}^*}$  is close to 0 eV for the  $\theta = 1/9$  structure under 1 and 1.5% tensile strain. Moreover, it is important to mention that the  $\theta = 9/9$  structure under 2% tensile strain has the minimum  $\Delta G_{\text{H}^*}$  of  $-0.132$  eV, which is still comparable with lots of 2D catalysis for HER,

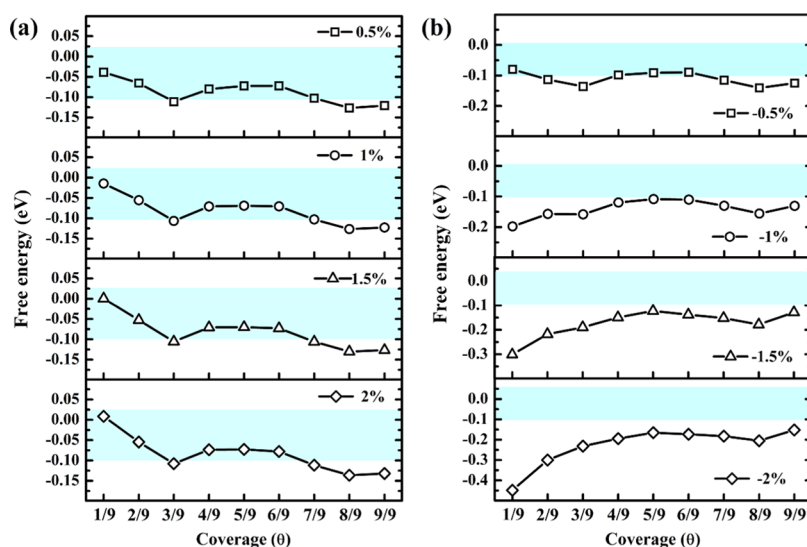


**Figure 7.** Variation of the free energies of hydrogen adsorption with applied biaxial strain. The free energy with catalytic activity comparable to that of Pt is highlighted in light blue.

revealing that the h-B<sub>2</sub>O monolayer maintains excellent catalytic performance even under tensile strain.

As depicted in Figure 7b, compressive strain drives  $\Delta G_{H^*}$  to move toward a more negative value, which could reduce the HER activity. Specifically, only  $\Delta G_{H^*}$  of  $\theta = 1/9, 4/9, 5/9$ , and  $6/9$  configurations under  $-0.5\%$  strain are very close to the thermoneutrality criterion. For the  $\theta = 8/9$  case, it has a relatively poor HER activity with  $\Delta G_{H^*} = -0.141$  eV. With regards to  $-1\%$  compressive strain, the evolution of the HER activity shifts distinctly. The maximum value of  $\Delta G_{H^*}$  is  $-0.108$  eV with  $\theta = 5/9$ . As the compressive strain increases to  $-2\%$ , the change of  $\Delta G_{H^*}$  can be ignored compared with the results under  $-1\%$  strain. In detail, the values of  $\Delta G_{H^*}$  of  $\theta = 9/9$  are  $-0.128$  and  $-0.152$  eV under  $-1.5$  and  $-2\%$  strain, respectively.

To get an insight into the adsorption action caused by strains, we calculated their DOS. For the h-B<sub>2</sub>O monolayer with a low H coverage ( $\theta = 1/9$ ), the Fermi level shifts up with the increasing strain, as shown in Figure S8a. Subsequently, the orbital hybridization between B and H atoms is to be reduced in the area between  $-4$  and  $-1$  eV, weakening the strength of the B–H bond. However, for the  $\theta = 9/9$  case in Figure S8b, it is clear that the electrons under the Fermi energy shift are mainly located in the area of  $-4$  to  $-1$  eV, which could increase the interaction between B and H atoms, resulting in the lower  $\Delta G_{H^*}$  as observed in Figure 7. Besides, we also explore the variation of work function ( $\Delta\Phi$ ) under strains for the hydrogen-adsorbed h-B<sub>2</sub>O monolayer. It is shown that increased hydrogen coverage could decelerate the release of electrons from the h-B<sub>2</sub>O monolayer, as shown in Figure 8. Moreover, with the  $\theta \leq 6/9$  cases, the release of electrons is easier with the transformation from compressive strain to tensile strain. However, the tensile strain results in a larger  $\Delta\Phi$  than the compressive strain for the  $\theta \geq 7/9$  cases. For example, the value of  $\Delta\Phi$  of the  $\theta = 9/9$  configuration is  $5.19$  eV at  $-2\%$  strain but  $5.3$  eV at  $2\%$  strains. This evolution can be concluded from the Fermi shift as well (Figure S8), in which the Fermi level moves to lower energy when the strain-driven shifts from compressive strain to tensile strain.

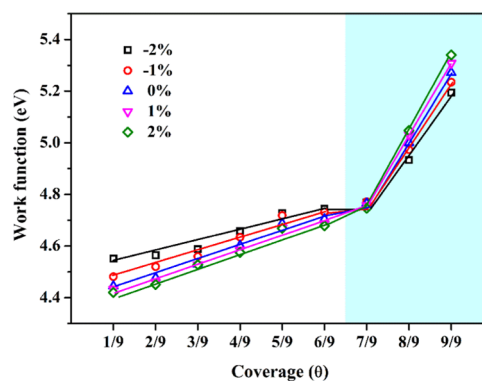


**Figure 8.** Evolution of the work function of the h-B<sub>2</sub>O monolayer driven by hydrogen coverage under different strains.

#### 4. CONCLUSIONS

In summary, based on the first-principles calculations, we have systematically investigated the ground structural property, electronic property, and photocatalytic performance of the h-B<sub>2</sub>O monolayer. Besides, the effects of hydrogen coverages and strains-driven on the HER catalytic activity has been studied. First, we confirmed that the B site of the h-B<sub>2</sub>O monolayer is a highly active site for HER compared with other possible active sites on the h-B<sub>2</sub>O monolayer and the B/O defective model. The calculated Gibbs free energy ( $\Delta G_{H^*}$ ) of the pristine h-B<sub>2</sub>O monolayer is  $-0.07$  eV with the adsorbed hydrogen, which is more favorable compared with the Pt catalyst ( $-0.09$  eV). The predicted catalytic activity of the h-B<sub>2</sub>O monolayer is quite robust with increasing hydrogen ratio, in which  $\Delta G_{H^*}$  is  $-0.03$  eV at the coverage  $\theta = 5/9$ , revealing that the h-B<sub>2</sub>O monolayer is quite suitable for HER catalysis even with high coverage. Additionally, we found that the tensile strains ( $0$ – $2\%$ ) have a positive effect on the HER activity of the h-B<sub>2</sub>O monolayer, resulting in  $\Delta G^*$  being close to  $0$  eV at low hydrogen coverage. However, the applied compressive strain could strengthen the bonding of hydrogen with the h-B<sub>2</sub>O monolayer, leading to lower values of  $\Delta G^*$ . After analyzing the DOS, we found that the hydrogen-absorbed h-B<sub>2</sub>O monolayer retains the metallic property, while increasing the hydrogen



coverage drives the Fermi level move toward the lower energy level. Moreover, the reaction kinetics suggest that the HER mechanism of the h-B<sub>2</sub>O monolayer should follow the Heyrovsky-dominated Volmer–Heyrovsky reaction.

## ■ ASSOCIATED CONTENT

### Supporting Information

The Supporting Information is available free of charge at <https://pubs.acs.org/doi/10.1021/acs.jpcc.0c00834>.

Calculated band structure of the h-B<sub>2</sub>O monolayer based on the PBE method; main projections of the band structures and the corresponding average projections weight; projected density of states for the h-B<sub>2</sub>O monolayer; the possible adsorption sites for hydrogen atom; advantageous location for hydrogen atom on the h-B<sub>2</sub>O monolayer and the B/O defect models; location of hydrogen coverages on the h-B<sub>2</sub>O monolayer; charge transfer ( $\Delta Q$ ) for adsorbed hydrogen atoms; projected density of state; and density of state of the h-B<sub>2</sub>O monolayer with adsorbed hydrogens under strains-driven (PDF)

## ■ AUTHOR INFORMATION

### Corresponding Authors

**Xiaoyong Yang** – State Key Laboratory for Environment-Friendly Energy Materials, Southwest University of Science and Technology, Mianyang 621010, P. R. China; Condensed Matter Theory Group, Materials Theory Division, Department of Physics and Astronomy, Uppsala University, 75120 Uppsala, Sweden; Email: [xiaoyong.yang@physics.uu.se](mailto:xiaoyong.yang@physics.uu.se)

**Rajeev Ahuja** – Condensed Matter Theory Group, Materials Theory Division, Department of Physics and Astronomy, Uppsala University, 75120 Uppsala, Sweden; Applied Materials Physics, Department of Materials and Engineering, Royal Institute of Technology (KTH), S-100 44 Stockholm, Sweden; [orcid.org/0000-0003-1231-9994](https://orcid.org/0000-0003-1231-9994); Email: [rajeev.ahuja@physics.uu.se](mailto:rajeev.ahuja@physics.uu.se)

### Authors

**Xiaofeng Zhao** – State Key Laboratory for Environment-Friendly Energy Materials and School of Materials Science and Engineering, Southwest University of Science and Technology, Mianyang 621010, P. R. China; Condensed Matter Theory Group, Materials Theory Division, Department of Physics and Astronomy, Uppsala University, 75120 Uppsala, Sweden; [orcid.org/0000-0003-1079-2833](https://orcid.org/0000-0003-1079-2833)

**Deobrat Singh** – Condensed Matter Theory Group, Materials Theory Division, Department of Physics and Astronomy, Uppsala University, 75120 Uppsala, Sweden; [orcid.org/0000-0001-7246-8743](https://orcid.org/0000-0001-7246-8743)

**Pritam Kumar Panda** – Condensed Matter Theory Group, Materials Theory Division, Department of Physics and Astronomy, Uppsala University, 75120 Uppsala, Sweden; [orcid.org/0000-0003-4879-2302](https://orcid.org/0000-0003-4879-2302)

**Wei Luo** – Condensed Matter Theory Group, Materials Theory Division, Department of Physics and Astronomy, Uppsala University, 75120 Uppsala, Sweden

**Yuxiang Li** – State Key Laboratory for Environment-Friendly Energy Materials and School of Materials Science and Engineering, Southwest University of Science and Technology, Mianyang 621010, P. R. China

Complete contact information is available at:

<https://pubs.acs.org/doi/10.1021/acs.jpcc.0c00834>

## Notes

The authors declare no competing financial interest.

## ■ ACKNOWLEDGMENTS

We sincerely appreciate the financial support of the National Natural Science Foundation of China (No. 11275158 and 11705152) and the Longshan academic talent research supporting program of Southwest University of Science and Technology (No. 17LZX407). X.Z. acknowledge financial support from the Southwest University of Science and Technology. X.Y. acknowledges to financial support from the China Scholarship Council. D.S. and R.A. thank Olle Engkvists stiftelse and Swedish Research Council (VR) for financial support. SNIC and HPC2N are acknowledged for providing the computing facilities.

## ■ REFERENCES

- (1) Gao, G.; O'Mullane, A. P.; Du, A. 2D MXenes: A New Family of Promising Catalysts for the Hydrogen Evolution Reaction. *ACS Catal.* **2017**, *7*, 494–500.
- (2) Ma, X.; Wu, X.; Wang, H.; Wang, Y. A Janus MoSSe Monolayer: A Potential Wide Solar-Spectrum Water-Splitting Photocatalyst with a Low Carrier Recombination Rate. *J. Mater. Chem. A* **2018**, *6*, 2295–2301.
- (3) Dong, Y.; Dang, J.; Wang, W.; Yin, S.; Wang, Y. First-Principles Determination of Active Sites of Ni Metal-Based Electrocatalysts for Hydrogen Evolution Reaction. *ACS Appl. Mater. Interfaces* **2018**, *10*, 39624–39630.
- (4) Yang, X.; Banerjee, A.; Xu, Z.; Wang, Z.; Ahuja, R. Interfacial Aspect of ZnTe/In<sub>2</sub>Te<sub>3</sub> Heterostructures as an Efficient Catalyst for Hydrogen Evolution Reaction. *J. Mater. Chem. A* **2019**, *7*, 27441–27449.
- (5) Nørskov, J. K.; Bligaard, T.; Logadottir, A.; Kitchin, J. R.; Chen, J. G.; Pandelov, S.; Stimming, U. Trends in the Exchange Current for Hydrogen Evolution. *J. Electrochem. Soc.* **2005**, *152*, No. J23.
- (6) Mir, S. H.; Chakraborty, S.; Jha, P. C.; Wärmå, J.; Soni, H.; Jha, P. K.; Ahuja, R. Two-Dimensional Boron: Lightest Catalyst for Hydrogen and Oxygen Evolution Reaction. *Appl. Phys. Lett.* **2016**, *109*, No. 053903.
- (7) Zhang, Z.; Yang, Y.; Gao, G.; Yakobson, B. I. Two-Dimensional Boron Monolayers Mediated by Metal Substrates. *Angew. Chem., Int. Ed.* **2015**, *54*, 13022–13026.
- (8) Links, R.; Stories, R. A Metal-Free Polymeric Photocatalyst for Hydrogen Production from Water under Visible Light. *Nat. Mater.* **2008**, *8*, 76–80.
- (9) Bhimanapati, G. R.; Lin, Z.; Meunier, V.; Jung, Y.; Cha, J.; Das, S.; Xiao, D.; Son, Y.; Strano, M. S.; Cooper, V. R.; et al. Recent Advances in Two-Dimensional Materials beyond Graphene. *ACS Nano* **2015**, *9*, 11509–11539.
- (10) Zhang, S.; Zhou, W.; Ma, Y.; Ji, J.; Cai, B.; Yang, S. A.; Zhu, Z.; Chen, Z.; Zeng, H. Antimonene Oxides: Emerging Tunable Direct Bandgap Semiconductor and Novel Topological Insulator. *Nano Lett.* **2017**, *17*, 3434–3440.
- (11) Milana, S. The Lab-to-Fab Journey of 2D Materials. *Nat. Nanotechnol.* **2019**, *14*, 919–921.
- (12) Schwierz, F. Graphene Transistors. *Nat. Nanotechnol.* **2010**, *5*, 487–496.
- (13) Li, D.; Kaner, R. B. Graphene-Based Materials. *Science* **2008**, *320*, 1170–1172.
- (14) Shu, H.; Zhou, D.; Li, F.; Cao, D.; Chen, X. Defect Engineering in MoSe<sub>2</sub> for the Hydrogen Evolution Reaction: From Point Defects to Edges. *ACS Appl. Mater. Interfaces* **2017**, *9*, 42688–42698.
- (15) Zeng, M.; Chen, Y.; Li, J.; Xue, H.; Mendes, R. G.; Liu, J.; Zhang, T.; Rummeli, M. H.; Fu, L. 2D WC Single Crystal Embedded

in Graphene for Enhancing Hydrogen Evolution Reaction. *Nano Energy* **2017**, *33*, 356–362.

(16) Manchanda, P.; Enders, A.; Sellmyer, D. J.; Skomski, R. Hydrogen-Induced Ferromagnetism in Two-Dimensional Pt Dichalcogenides. *Phys. Rev. B* **2016**, *94*, No. 104426.

(17) Lei, S.; Wang, X.; Li, B.; Kang, J.; He, Y.; George, A.; Ge, L.; Gong, Y.; Dong, P.; Jin, Z.; et al. Surface Functionalization of Two-Dimensional Metal Chalcogenides by Lewis Acid-Base Chemistry. *Nat. Nanotechnol.* **2016**, *11*, 465–471.

(18) Akinwande, D.; Brennan, C. J.; Bunch, J. S.; Egberts, P.; Felts, J. R.; Gao, H.; Huang, R.; Kim, J.-S.; Li, T.; Li, Y.; et al. A Review on Mechanics and Mechanical Properties of 2D Materials—Graphene and Beyond. *Extreme Mech. Lett.* **2017**, *13*, 42–77.

(19) Tan, C.; Cao, X.; Wu, X.-J.; He, Q.; Yang, J.; Zhang, X.; Chen, J.; Zhao, W.; Han, S.; Nam, G.-H.; et al. Recent Advances in Ultrathin Two-Dimensional Nanomaterials. *Chem. Rev.* **2017**, *117*, 6225–6331.

(20) Krajewska, A.; Oberda, K.; Azpeitia, J.; Gutierrez, A.; Pasternak, I.; López, M. F.; Mierczyk, Z.; Munuera, C.; Strupinski, W. Influence of Au Doping on Electrical Properties of CVD Graphene. *Carbon* **2016**, *100*, 625–631.

(21) Wu, H.-H.; Huang, H.; Zhong, J.; Yu, S.; Zhang, Q.; Zeng, X. C. Monolayer Triphosphates  $MP_3$  ( $M = \text{Sn, Ge}$ ) with Excellent Basal Catalytic Activity for Hydrogen Evolution Reaction. *Nanoscale* **2019**, *11*, 12210–12219.

(22) Zhang, C.; Li, Y.; Shuai, D.; Shen, Y.; Xiong, W.; Wang, L. Graphitic Carbon Nitride ( $g\text{-C}_3\text{N}_4$ )-Based Photocatalysts for Water Disinfection and Microbial Control: A Review. *Chemosphere* **2019**, *214*, 462–479.

(23) Jiang, J.; Ou-Yang, L.; Zhu, L.; Zheng, A.; Zou, J.; Yi, X.; Tang, H. Dependence of Electronic Structure of  $g\text{-C}_3\text{N}_4$  on the Layer Number of Its Nanosheets: A Study by Raman Spectroscopy Coupled with First-Principles Calculations. *Carbon* **2014**, *80*, 213–221.

(24) Hu, J.; Ji, Y.; Mo, Z.; Li, N.; Xu, Q.; Li, Y.; Xu, H.; Chen, D.; Lu, J. Engineering Black Phosphorus to Porous  $g\text{-C}_3\text{N}_4$ -Metal-Organic Framework Membrane: A Platform for Highly Boosting Photocatalytic Performance. *J. Mater. Chem. A* **2019**, *7*, 4408–4414.

(25) Zhu, B.; Xia, P.; Ho, W.; Yu, J. Isoelectric Point and Adsorption Activity of Porous  $g\text{-C}_3\text{N}_4$ . *Appl. Surf. Sci.* **2015**, *344*, 188–195.

(26) Ling, F.; Li, W.; Ye, L. The Synergistic Effect of Non-Metal Doping or Defect Engineering and Interface Coupling on the Photocatalytic Property of  $g\text{-C}_3\text{N}_4$ : First-Principle Investigations. *Appl. Surf. Sci.* **2019**, *473*, 386–392.

(27) Li, W.; Kong, L.; Chen, C.; Gou, J.; Sheng, S.; Zhang, W.; Li, H.; Chen, L.; Cheng, P.; Wu, K. Experimental Realization of Honeycomb Borophene. *Sci. Bull.* **2018**, *63*, 282–286.

(28) Qian, X.; Liu, J.; Fu, J.; Li, J. Quantum Spin Hall Effect in Two-Dimensional Transition Metal Dichalcogenides. *Science* **2014**, *346*, 1344–1347.

(29) Choi, W.; Choudhary, N.; Han, G. H.; Park, J.; Akinwande, D.; Lee, Y. H. Recent Development of Two-Dimensional Transition Metal Dichalcogenides and Their Applications. *Mater. Today* **2017**, *20*, 116–130.

(30) Zhao, Y.; Zhao, J. Functional Group-Dependent Anchoring Effect of Titanium Carbide-Based MXenes for Lithium-Sulfur Batteries: A Computational Study. *Appl. Surf. Sci.* **2017**, *412*, 591–598.

(31) Oh, W.-D.; Chang, V. W. C.; Hu, Z.-T.; Goei, R.; Lim, T. T. Enhancing the Catalytic Activity of  $g\text{-C}_3\text{N}_4$  through Me Doping ( $\text{Me} = \text{Cu, Co and Fe}$ ) for Selective Sulfathiazole Degradation via Redox-Based Advanced Oxidation Process. *Chem. Eng. J.* **2017**, *323*, 260–269.

(32) Xu, D.; Cheng, B.; Wang, W.; Jiang, C.; Yu, J.  $\text{Ag}_2\text{CrO}_4/g\text{-C}_3\text{N}_4/\text{Graphene Oxide}$  Ternary Nanocomposite Z-Scheme Photocatalyst with Enhanced  $\text{CO}_2$  Reduction Activity. *Appl. Catal., B* **2018**, *231*, 368–380.

(33) Novotný, M.; Domínguez-Gutiérrez, F. J.; Krstić, P. A Computational Study of Hydrogen Detection by Borophene. *J. Mater. Chem. C* **2017**, *5*, 5426–5433.

(34) Shi, L.; Ling, C.; Ouyang, Y.; Wang, J. High Intrinsic Catalytic Activity of Two-Dimensional Boron Monolayers for the Hydrogen Evolution Reaction. *Nanoscale* **2017**, *9*, 533–537.

(35) Zhang, Z.; Penev, E. S.; Yakobson, B. I. Two-Dimensional Boron: Structures, Properties and Applications. *Chem. Soc. Rev.* **2017**, *46*, 6746–6763.

(36) Wu, H.; Li, X.; Zhang, R.; Yang, J. Proposal of a Stable  $\text{B}_3\text{S}$  Nanosheet as an Efficient Hydrogen Evolution Catalyst. *J. Mater. Chem. A* **2019**, *7*, 3752–3756.

(37) Zhang, R.; Li, Z.; Yang, J. Two-Dimensional Stoichiometric Boron Oxides as a Versatile Platform for Electronic Structure Engineering. *J. Phys. Chem. Lett.* **2017**, *8*, 4347–4353.

(38) Wang, Z.-Q.; Lü, T.-Y.; Wang, H.-Q.; Feng, Y. P.; Zheng, J.-C. Review of Borophene and Its Potential Applications. *Front. Phys.* **2019**, *14*, No. 33403.

(39) Alvarez-Quiceno, J. C.; Miwa, R. H.; Dalpian, G. M.; Fazzio, A. Oxidation of Free-Standing and Supported Borophene. *2D Mater.* **2017**, *4*, No. 025025.

(40) Lherbier, A.; Rafael Botello-Méndez, A.; Charlier, J.-C. Electronic and Optical Properties of Pristine and Oxidized Borophene. *2D Mater.* **2016**, *3*, No. 045006.

(41) Chen, Y.; Yu, G.; Chen, W.; Liu, Y.; Li, G.-D.; Zhu, P.; Tao, Q.; Li, Q.; Liu, J.; Shen, X.; et al. Highly Active, Nonprecious Electrocatalyst Comprising Borophene Subunits for the Hydrogen Evolution Reaction. *J. Am. Chem. Soc.* **2017**, *139*, 12370–12373.

(42) Zhong, C.; Wu, W.; He, J.; Ding, G.; Liu, Y.; Li, D.; Yang, S. A.; Zhang, G. Two-Dimensional Honeycomb Borophene Oxide: Strong Anisotropy and Nodal Loop Transformation. *Nanoscale* **2019**, *11*, 2468–2475.

(43) Kresse, G.; Furthmüller, J. Efficient Iterative Schemes for Ab Initio Total-Energy Calculations Using a Plane-Wave Basis Set. *Phys. Rev. B* **1996**, *54*, 11169–11186.

(44) Kresse, G.; Furthmüller, J. Efficiency of Ab-Initio Total Energy Calculations for Metals and Semiconductors Using a Plane-Wave Basis Set. *Comput. Mater. Sci.* **1996**, *6*, 15–50.

(45) Blöchl, P. E. Projector Augmented-Wave Method. *Phys. Rev. B* **1994**, *50*, 17953–17979.

(46) Perdew, J. P.; Ernzerhof, M.; Burke, K. Rationale for Mixing Exact Exchange with Density Functional Approximations. *J. Chem. Phys.* **1996**, *105*, 9982–9985.

(47) Perdew, J. P.; Burke, K.; Ernzerhof, M. Generalized Gradient Approximation Made Simple. *Phys. Rev. Lett.* **1996**, *77*, 3865–3868.

(48) Grimme, S. Semiempirical GGA-type Density Functional Constructed with a Long-range Dispersion Correction. *J. Comput. Chem.* **2006**, *27*, 1787–1799.

(49) Heyd, J.; Scuseria, G. E.; Ernzerhof, M. Hybrid Functionals Based on a Screened Coulomb Potential. *J. Chem. Phys.* **2003**, *118*, 8207–8215.

(50) Henkelman, G.; Uberuaga, B. P.; Jónsson, H. Climbing Image Nudged Elastic Band Method for Finding Saddle Points and Minimum Energy Paths. *J. Chem. Phys.* **2000**, *113*, 9901–9904.

(51) Stace, A. J. A Measurement of the Average Kinetic Energy Released during the Unimolecular Decomposition of Argon Ion Clusters. *J. Chem. Phys.* **1986**, *85*, 5774–5778.

(52) Tsai, C.; Abild-Pedersen, F.; Nørskov, J. K. Tuning the  $\text{MoS}_2$  Edge-Site Activity for Hydrogen Evolution via Support Interactions. *Nano Lett.* **2014**, *14*, 1381–1387.

(53) Tan, T. L.; Wang, L.-L.; Johnson, D. D.; Bai, K. Hydrogen Deposition on Pt (111) during Electrochemical Hydrogen Evolution from a First-Principles Multiadsorption-Site Study. *J. Phys. Chem. C* **2013**, *117*, 22696–22704.

(54) Chianelli, R. R.; Berhault, G.; Raybaud, P.; Kasztelan, S.; Hafner, J.; Toulhoat, H. Periodic Trends in Hydrodesulfurization: In Support of the Sabatier Principle. *Appl. Catal., A* **2002**, *227*, 83–96.

(55) Pandey, M.; Thygesen, K. S. Two-Dimensional MXenes as Catalysts for Electrochemical Hydrogen Evolution: A Computational Screening Study. *J. Phys. Chem. C* **2017**, *121*, 13593–13598.

(56) Li, H.; Tsai, C.; Koh, A. L.; Cai, L.; Contryman, A. W.; Fragapane, A. H.; Zhao, J.; Han, H. S.; Manoharan, H. C.; Abild-



Pedersen, F.; et al. Activating and Optimizing MoS<sub>2</sub> Basal Planes for Hydrogen Evolution through the Formation of Strained Sulphur Vacancies. *Nat. Mater.* **2016**, *15*, 48–53.

(57) You, B.; Tang, M. T.; Tsai, C.; Abild-Pedersen, F.; Zheng, X.; Li, H. Enhancing Electrocatalytic Water Splitting by Strain Engineering. *Adv. Mater.* **2019**, *31*, No. 1807001.

(58) Banerjee, A.; Chakraborty, S.; Jena, N. K.; Ahuja, R. Scrupulous Probing of Bifunctional Catalytic Activity of Borophene Monolayer: Mapping Reaction Coordinate with Charge Transfer. *ACS Appl. Energy Mater.* **2018**, *1*, 3571–3576.

(59) Liu, C.; Dai, Z.; Zhang, J.; Jin, Y.; Li, D.; Sun, C. Two-Dimensional Boron Sheets as Metal-Free Catalysts for Hydrogen Evolution reaction. *J. Phys. Chem. C* **2018**, *122*, 19051–19055.

(60) Ma, X.; Lv, Y.; Xu, J.; Liu, Y.; Zhang, R.; Zhu, Y. A Strategy of Enhancing the Photoactivity of g-C<sub>3</sub>N<sub>4</sub> via Doping of Nonmetal Elements: A First-Principles Study. *J. Phys. Chem. C* **2012**, *116*, 23485–23493.

(61) Sinthika, S.; Waghmare, U. V.; Thapa, R. Structural and Electronic Descriptors of Catalytic Activity of Graphene-Based Materials: First-Principles Theoretical Analysis. *Small* **2018**, *14*, No. 1703609.